Remote Sensing of Environment 294 (2023) 113620

Contents lists available at ScienceDirect

Remote Sensing of Environment

journal homepage: www.elsevier.com/locate/rse

Inferring slip-surface geometry and volume of creeping landslides based on InSAR: A case study in Jinsha River basin

Ya Kang [a], Zhong Lu [b,*], Chaoying Zhao [c], Wei Qu [c]

[a] School of Geographic and Biologic Information, Nanjing University of Posts and Telecommunications, Nanjing 210023, China
[b] Roy M. Huffington Department of Earth Sciences, Southern Methodist University, Dallas, TX 75275, USA
[c] School of Geological Engineering and Geomatics, Chang'an University, Xi'an 710054, China

ARTICLE INFO

Edited by Jing M. Chen

Keywords:
Interferometric Synthetic Aperture Radar (InSAR)
Three-dimensional deformation
Landslide slip-surface
Landslide geometry
Landslide volume
Land mechanism
Jinsha River

ABSTRACT

The slip-surface geometry and volume of landslides are fundamental for landslide modeling and mechanism interpretation. The movement of a landslide, which is generally controlled by the slip-surface geometry, can be obtained from interferometric synthetic aperture radar (InSAR) measurements. However, there is a lack of a general approach for inferring the slip-surface geometry and volume of landslides through the InSAR-derived deformation field. Here we developed a geometry-based method to determine the landslide slip-surface geometry and volume using InSAR measurements and applied it to the Jinsha River Basin, a landslide-prone area that poses a significant threat to residents and infrastructure. Through the InSAR-derived displacement, topography, and Google Earth images, 50 creeping landslides were identified in the study area. Based on the displacement field, the landslide slip-surface slope was inverted under the assumption that the landslide displacement was parallel to the slip-surface. Then the two-dimensional slip-surface depths and volumes of selected landslides were inferred using the slip-surface slope. Comparisons with the in-situ data suggest that the results obtained in this study are reliable. The mapped landslides in the study area have depths of approximately 16–160 m along the central axis and volumes ranging from 483,412 to 135,789,944 m^3. The derived volume–area relationship and 2D slip-surface depth suggest that deep-seated landslide is a major landslide type in the study area. We conclude that our method can infer the slip-surface geometry of creeping landslides based on InSAR observation and our results have improved the understanding of the landslide mechanisms in the Jinsha River Basin, China.

1. Introduction

Major natural disasters triggered by landslides cause substantial economic losses and claim thousands of lives death every year in the world. Landslide identification and monitoring are prerequisites for hazard prevention (Zhao et al., 2012). Many studies detected and monitored landslides based on the surface displacement (e.g., (Kang et al., 2021)), because potential landslides usually experience a longtime creeping stage before their final failure, and some can last for years or even decades. Surface displacement can also reflect the geometrical characteristics of the slip-surface of landslides (Schlögel et al., 2015).

The geometry of the slip-surface, defined by its direction, depth, and shape, provides critical data support for landslide stability analysis and mechanism interpretation (Carter & Bentley, 1985; Xu et al., 2022). Because the detailed slip-surface slope can also reflect the shape of the slip-surface, it has been used in landslide classification (e.g. (Crippa et al., 2021; Saroli et al., 2021)). The slip-surface geometry can also be used to derive the landslide volume, which is one of the most important parameters to control landslide propagation distance, the affected area, and potential damages after failure (Jaboyedoff et al., 2020). Decades ago, some studies had already inferred the two-dimensional (2D) slip-surface geometry based on ground-surface displacement (e.g., (Bishop, 1999; Carter & Bentley, 1985)). In recent years, remote sensing technology, which can obtain detailed ground-surface displacement, has provided new constraints for slip-surface geometry inversion (Booth et al., 2020; Jaboyedoff et al., 2020). As a microwave remote sensing technology, InSAR is not only a powerful tool for landslide detection and monitoring but also shows the potential in inferring the geometry of the slip-surface (Handwerger et al., 2021; Lu & Kim, 2021). For example, based on rheology, some studies have used InSAR measurements to retrieve the detailed slip-surface depths, which can directly reflect the slip-surface geometry (e.g., (Hu et al., 2018)). However, the rheology-

* Corresponding author.
E-mail address: zhonglu@smu.edu (Z. Lu).

https://doi.org/10.1016/j.rse.2023.113620
Received 20 October 2022; Received in revised form 22 April 2023; Accepted 6 May 2023
Available online 14 May 2023

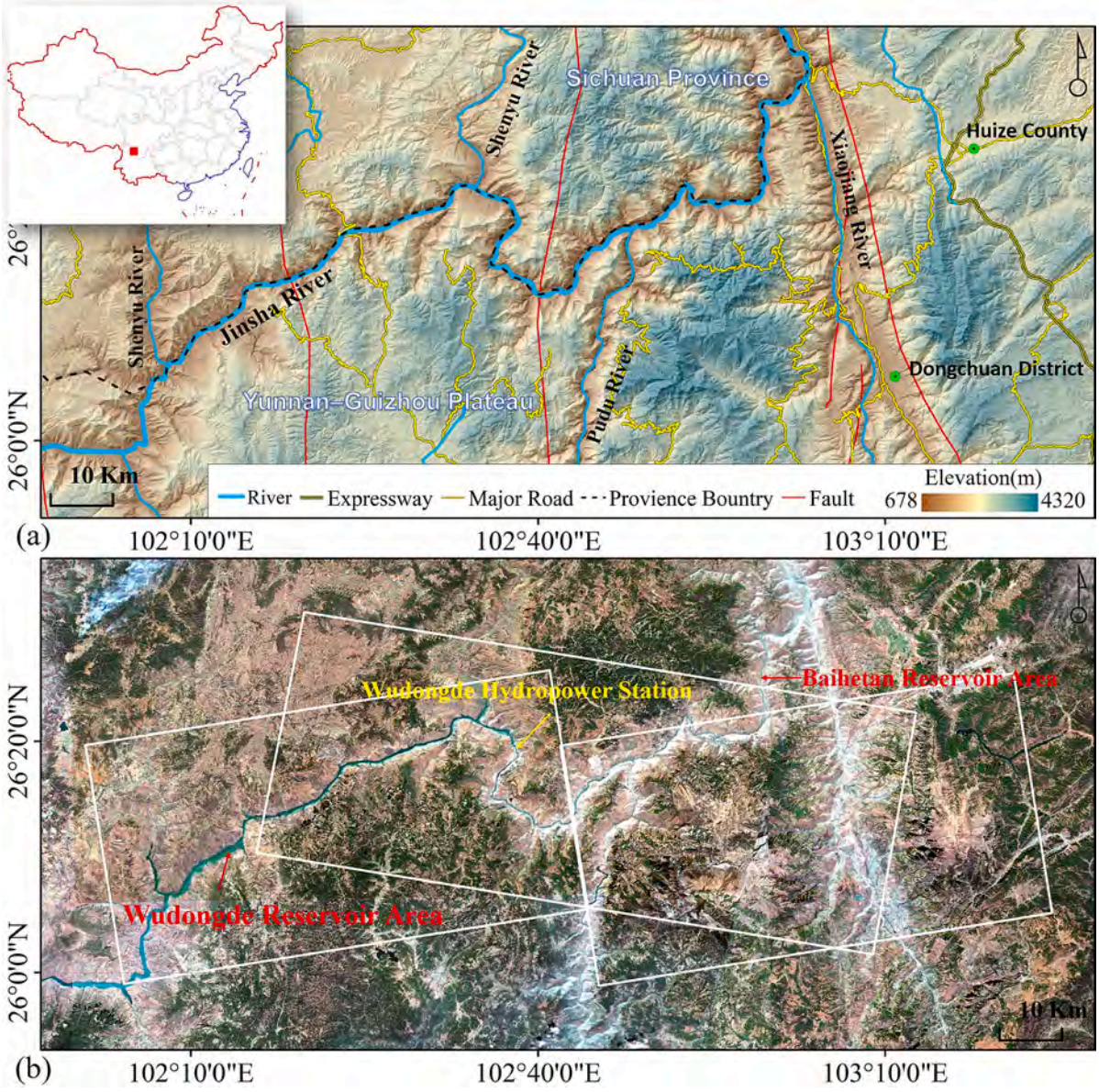

Fig. 1. (a) The location and terrain of the study area. (b) Optical remote sensing images from Sentinel-2 acquired from November 2020 to February 2021; the white rectangle shows the SAR coverage. The inset shows the location of the study area.

based method typically requires prior knowledge about the rheological property of the landslide body and depth measurement at one location. Under the assumption that the displacement vector of a landslide is parallel to its slip-surface, some studies have used a vector inclination method to plot the slip-surface along a profile based on InSAR-derived three-dimensional (3D) displacements (Intrieri et al., 2020); however, this geometry-based method only acquires 2D slip-surface geometry along a profile. Several studies have attempted to estimate the slip-surface inclination through east-west and vertical (2D) displacement derived from InSAR (e.g., (Crippa et al., 2021; Saroli et al., 2021)), but this method cannot accurately reflect the actual slip-surface slope. Hence, there is a lack of general methods for landslide volume estimation based on InSAR (Jaboyedoff et al., 2020).

The Jinsha River is located in the upper reaches of the Yangtze River. During river cutting in the Jinsha River Basin, many V-shaped canyons with large elevation drops were formed (Wang, 2013). Both sides of the canyons are eroded by precipitation and rivers, resulting in devastating geological disasters including landslides and mudslides (Xu, 2013). Many hydropower stations have been built or planned on this river to utilize hydraulic resources. We selected a region partly covering the reservoir areas of the Wudongde and Baihetan Hydropower Stations as the study site (Fig. 1). It is located in the transition zone between the mountainous area of southwestern Sichuan Province and the Yunnan–Guizhou Plateau belonging to the southeastern margin of the Qinghai–Tibet Plateau (Xu, 2013). The topographic relief is too huge, with a maximum height difference of 3642 m. The vegetation coverage is so uneven that more exposed surfaces are found in the river valleys and the flat regions, and more vegetation coverage in the mountainous areas. The study area has a subtropical monsoon climate, and precipitation is mainly concentrated in summer (June to October) (Xu, 2013).

A super-large hydropower station (the Wudongde Hydropower Station) and several major roads are located in this region (Fig. 1). Landslides and debris flows may cause massive damage to the dam, threatening the safety of people in the reservoir area (Huang et al., 2012). Although InSAR-based landslide identification and monitoring has been conducted in this area (Zhao et al., 2018), only a few studies have investigated the geometric slip-surface information of individual landslides based on geological surveys. Therefore, we designed a

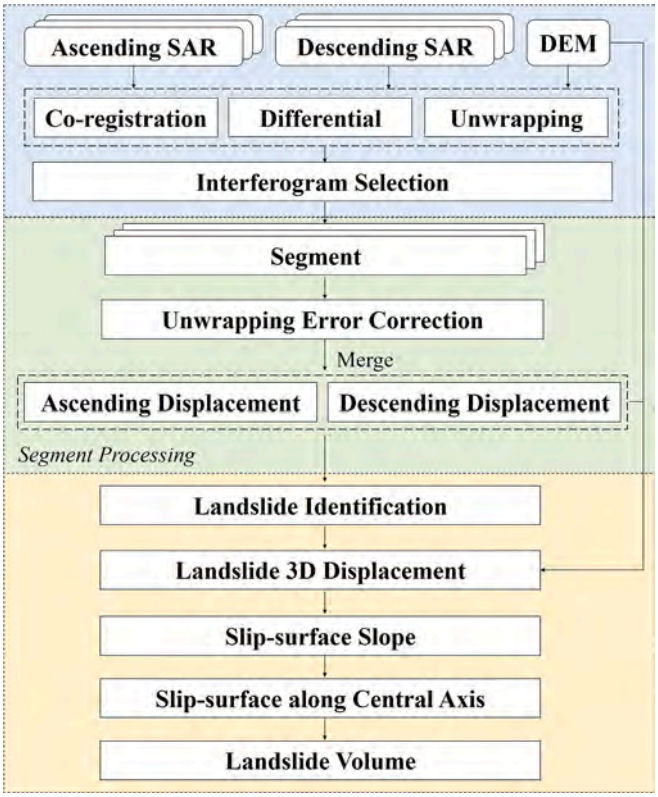

Fig. 2. The flow chart of the landslide slip-surface geometry and volume estimation.

geometry-based strategy to infer the slip-surface geometry and volume of the landslide in an area of the Jinsha River Basin by using the InSAR measurements.

2. Methodology

A set of processes was designed to estimate the slip-surface geometry and volume of the landslides in the study area (Fig. 2). Firstly, based on the SAR data with ascending and descending tracks, the surface displacements of the research area were estimated through the InSAR segment processing (Kang et al., 2021). Then, the active landslides in the study area were identified by the InSAR measurements, Google-Earth image and Digital Elevation Model (DEM) (Zhao et al., 2018). Finally, based on the 3D displacements derived from InSAR, the slip-surface geometry and volume of the landslide were estimated under the assumption that the displacements are parallel to the slip-surface and by using an elliptical paraboloid-based model respectively (Carter & Bentley, 1985; Hu et al., 2018). The details of these methods were presented as follows.

2.1. InSAR line-of-sight processing and landslide identification

In this study, 91 Sentinel-1 images with ascending tracks and 88 Sentinel-1 images with descending tracks from March 2018 to March 2021 were collected and processed. We set the thresholds of the temporal and spatial baselines as 36 days and 300 m, respectively to generate interferograms avoiding decorrelation. And only the interferograms with relatively high effective coherence ratios were subjected to further processing. The effective coherence ratio refers to the percentage of the area in which coherence is higher than a critical threshold (Kang et al., 2021). Typically, this threshold can be set as the average coherence of the water-covered and shadowed areas. In this study, the average coherence of the shadowed areas (0.1) was set as the critical coherence, and the effective coherence ratio was set as 0.7, to select interferograms of high quality. The configurations of the selected interferograms are shown in Fig. 3. The multi-look ratio of the images was set to 4:1, which resulted in an image resolution of ~20 m in both directions. The 1-arc-second Shuttle Radar Topography Mission (SRTM) digital elevation model (DEM) was used to remove the topographic phase, geocode the results, and segment the interferograms.

Because the study area is mountainous, interferograms are often disturbed by severe atmospheric noise. To attenuate the impact of atmospheric delay, segment processing was used to obtain the linear deformation rate (Kang et al., 2021). Since vertically stratified components of tropospheric delays are difficult to estimate accurately over sizable spatial scales or large elevation variations, the tropospheric delay was estimated in local windows/segments (Bekaert et al., 2015). The surface displacement was calculated in each segment independently, and these segment results were merged (Kang et al., 2021).

In addition to the atmospheric noise, we found that some interferograms cannot be unwrapped correctly because of the large displacement gradients of the landslides in the study area. Therefore, we designed a phase-closure method to correct the unwrapping errors in the segment processing, and this step was placed after the interferogram segmentation. As the cumulative movements of creeping landslides gradually increase, the unwrapping errors increasingly occur in pairs with longer temporal baselines (Wang et al., 2012). Therefore, a phase-closure technique based on non-redundant measurements was used to correct the unwrapping errors. The main difference between our method and the one used in the π-RATE method (Wang et al., 2012) is that a chain of interferograms with the shortest possible temporal baselines was selected as the redundant measurements to correct the unwrapping errors caused by dense fringes corresponding to large displacement. The flow of the proposed method for a generic pixel is described briefly

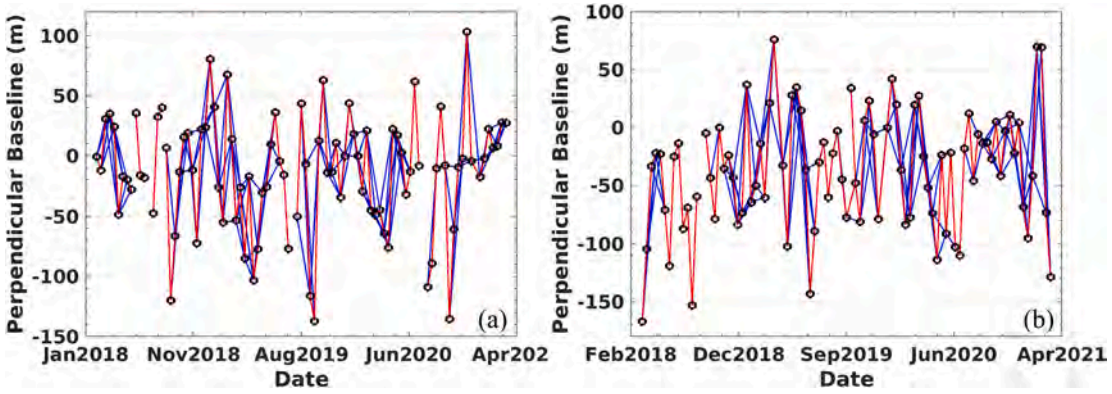

Fig. 3. The configuration of the temporal and spatial baseline: (a) ascending dataset; (b) descending dataset. The red line represents the non-redundant measurement. (For interpretation of the references to colour in this figure legend, the reader is referred to the web version of this article.)

below:

(i) Non-redundant measurements were selected using the minimum spanning tree algorithm (Kruskal, 1956). To avoid the non-redundant measurements containing unwrapping errors, a chain of interferograms (red line in Fig. 3) was constructed.

(ii) The closure of the redundant measurements was constructed using the non-redundant measurements (Wang et al., 2012). In our method, these residuals $\rho = (\rho_1 \ \rho_2 \ \cdots \ \rho_n)$ were calculated by using the following formula based on least squares adjustment for solving time-series deformation:

$$\rho = \varphi - B\phi \tag{1}$$

$$\phi = \left(B_{non}^T B_{non}\right)^{-1} B_{non}^T \varphi_{non} \tag{2}$$

where ϕ represents a series of cumulative phases estimated from the non-redundant interferograms; φ represents the unwrapped interferometric phase; B represents the design matrix, which consists of −1, 0, and 1: this is because the interferometric phase $\varphi_{\omega,\eta} = \phi_\eta - \phi_\omega$, where η and ω represent the acquisition time of two SAR images, respectively. The subscript *non* indicates the non-redundant measurements. If the i^{th} residual ρ_i was greater than three times the root mean square error of ρ, the measurement φ_i was considered to contain an unwrapping error and the residual ρ_i was used to correct it. It has been noted that L1-norm can be advantageous in suppressing the influences of outliers (e.g., (Lauknes et al., 2010)). So, in addition to the least squares, L1-norm can be explored to estimate the residual.

(iii) Temporal coherence was used to evaluate the effect of the correction (Lauknes et al., 2010). If the temporal coherence decreased after the correction, the original unwrapped phase was left for subsequent processing.

Following the InSAR segment processing, landslides were identified based on their deformation patterns, which can be plotted on DEM and/or optical remote sensing images. In the identification, we used the DEM to exclude land subsidence interference (Zhao et al., 2012). The Google Earth images are used to roughly depict the extent of the landslides, guided by the InSAR measurements (Zhao et al., 2018). Because obvious deformation may only occur in some parts of the landslide region during a specific InSAR monitoring period, and the boundaries of some landslides (groove, crack or discontinuity of stratum) can be identified using optical remote sensing images (Wang et al., 2011).

2.2. 3D displacement inversion

As it is limited by the imaging geometry of SAR satellites, spaceborne InSAR is not sensitive to north–south displacements (Hu et al., 2018). Therefore, some basic assumptions are proposed for multi-dimensional displacement inversion over landslides (Hu et al., 2018; Liu et al., 2021). In InSAR-based landslide 3D displacement inversion, some studies assume that the slip-surface is parallel to the ground surface (Liu et al., 2021), which makes the 3D displacement of landslides derived from InSAR measurements entirely parallel to the ground surface. However, not all landslides have a slip-surface parallel to the ground surface (e.g., rotational and multiple rotational landslides). When inverting the 3D displacement of a landslide based on datasets with both ascending and descending tracks, rather than assuming the slip-surface is parallel to the ground surface slope, we only assume that the landslide movement in the horizontal direction is consistent with the slope aspect (Hu et al., 2018). Hence, the transverse deformation of the landslide in the computation was neglected (Baum et al., 1998; Hu et al., 2018). Under this assumption, the 3D displacement can be inverted using the following equation.

$$L\begin{bmatrix} v_N \\ v_E \\ v_U \end{bmatrix} = \begin{bmatrix} v_{asc} \\ v_{dec} \\ 0 \end{bmatrix} \tag{3}$$

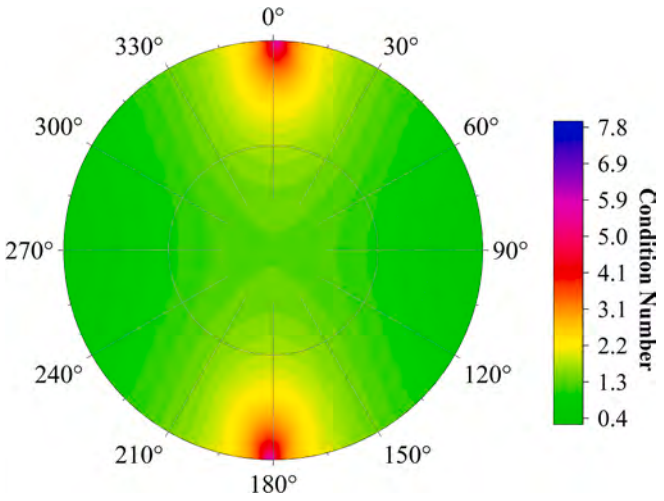

Fig. 4. The logarithm transformed ($\log_{10}$) condition number versus with the slope aspect.

where $L = [l_{asc} \quad l_{dec} \quad s_\tau]^T$, v indicates the displacement, the subscripts E, N, and U indicate north, east and vertical directions, respectively; the subscripts *asc* and *dec* indicate the ascending and descending tracks; $l = [sin\theta sin\alpha \quad -sin\theta cos\alpha \quad cos\theta]$, where θ is the incidence angle and α is the satellite heading angle; $s_\tau = [sin\beta_{asp} \quad -cos\beta_{asp} \quad 0]$, where β_{asp} represents the slope aspect. In addition, to reduce the interference of local topographic relief, we set the average slope aspect of each creeping body as its horizontal sliding direction. The condition number of the design matrix L can be used to evaluate the sensitivity of the linear equations in Eq. (3) to the noise. A large condition number usually means that the inverted result is unreliable. We calculated the condition numbers of Eq. (3) for different slope aspects. As shown in Fig. 4, when the landslide moves in a near north–south direction, the condition number is huge, which indicates that Eq. (3) still cannot be used to invert the 3D displacement of a landslide sliding in a near north–south direction. Therefore, it is necessary to evaluate the precision of the 3D displacement of the landslides. According to the error propagation law, the uncertainty of the Quasi-3D displacement can be obtained by:

$$M_{3D} = L^{-1} M_{LOS} \left(L^{-1}\right)^T \tag{4}$$

in which M indicates the covariance matrix $M_{LOS} = \Lambda\left(m_{asc}^2 \quad m_{dec}^2 \quad 0\right)$, Λ represents a diagonal matrix, and m is the standard deviation of the

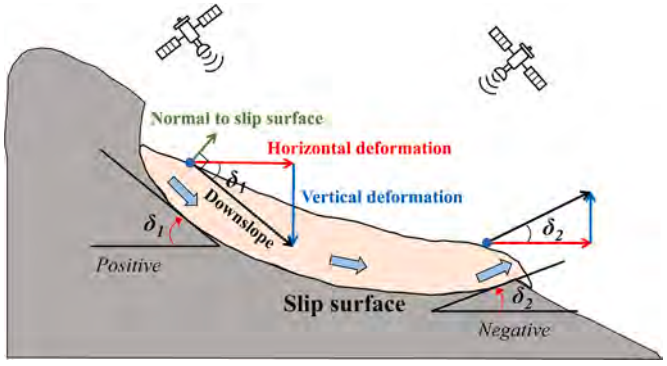

Fig. 5. The conceptual model for inverting the slope of a slip-surface. The downslope direction is parallel to the slip-surface. We stipulate that when the horizontal line rotates downward to be tangent to the slip-surface, the slope of the slip-surface is positive (δ_1). In contrast, when the horizontal line rotates upward to be tangent to the slip-surface, the slope of the slip-surface is negative (δ_2).

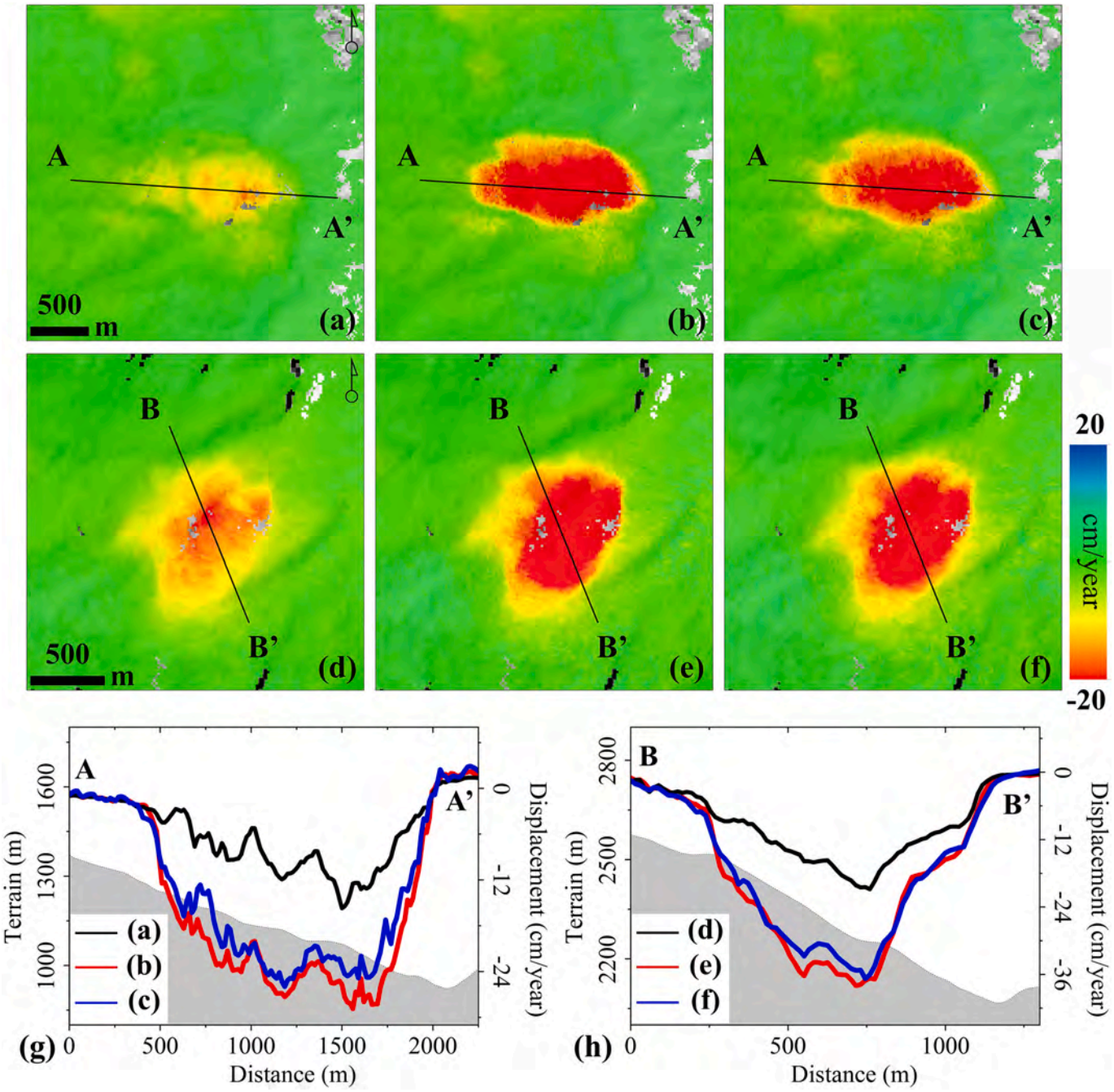

Fig. 6. Results for two landslides with large displacement in the study area. (a, d) Linear displacement rates without unwrapping error correction; (b, e) Linear displacement rates acquired from the interferograms corrected by the phase-closure technique; (c, f) Linear displacement rates acquired from manually selected interferograms that have a lower probability of phase unwrapping errors; (g, h) Cross-sections of the displacement rates and the terrain.

linear deformation rate in the line-of-sight (LOS) direction.

2.3. Slip-surface slope inversion

Under the assumption that the displacement vector is parallel to the slip-surface, Carter and Bentley (Carter & Bentley, 1985) inferred landslide thickness along a profile using surface displacement. They found that the accuracy of the inferred thickness could reach approximately 2% of the distance between ground measurements (Carter & Bentley, 1985). Baum et al. (Baum et al., 1998) verified that the displacement at the ground surface was roughly parallel to the slip-surface of the landslide. It should be noted that, in this study, the ground-surface slope was not used in the 3D displacement inversion (as shown in Section 2.2). In addition, for landslides with small length-depth ratios, the depth-averaged landslide velocity vector is typically proportional to the ground-surface horizontal velocity vector (Handwerger et al., 2021). Therefore, the detailed slope of the slip-surface can be estimated using the inverted 3D displacement, under the assumption that the displacement vector is parallel to the slip-surface. The conceptual model of the slip-surface slope inversion is shown in Fig. 5; if the landslide body slides along a continuous slip-surface and the displacement in the downslope direction is much larger than the displacement in the slope-normal directions (the direction normal to the slip-surface), the angle between the horizontal and vertical displacement is inferred as the slope of the slip-surface. Then the slope of the slip-surface can be calculated as,

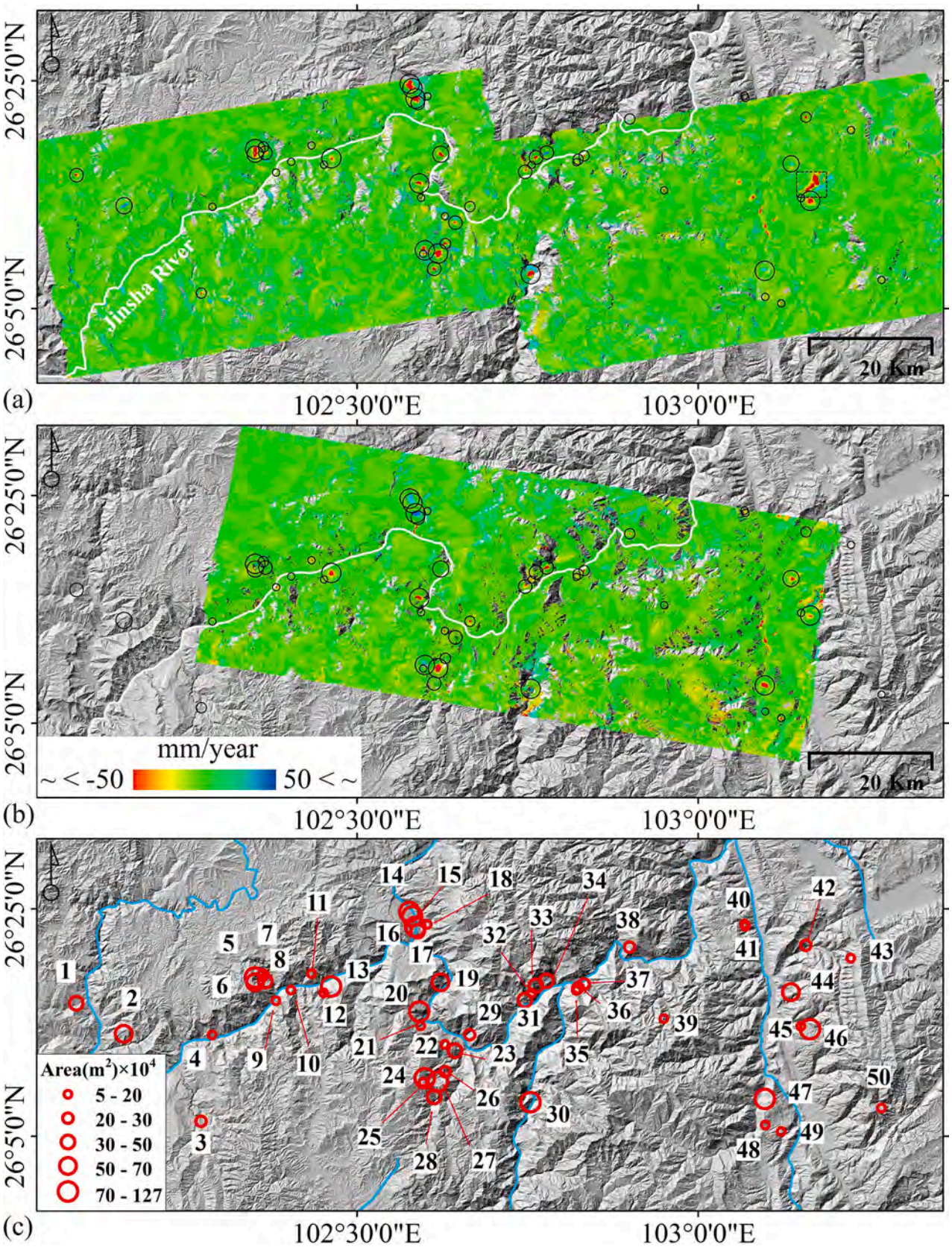

Fig. 7. (a) Linear displacement rate in line-of-sight (LOS) direction from the ascending track. The landslides in the dashed rectangle were not numbered. (b) Linear displacement rate in the LOS direction from the descending track. (c) The location and number of the detected landslides. In the figure, red (negative) and blue (positive) indicate movement away from and toward the satellite, respectively. The size of the circle reflects the area of the landslide, and the blue lines represent the Jinsha River and its tributaries. (For interpretation of the references to colour in this figure legend, the reader is referred to the web version of this article.)

$$\delta = arctan\left(-v_U \Big/ \sqrt{v_N^2 + v_E^2}\right) \tag{5}$$

The landslide direction has a significant impact on the precision of the inverted 3D displacements (shown in Section 2.2). Specifically, the precision becomes unacceptable when it slides in a near north–south direction. Therefore, it is necessary to evaluate the precision of the slip-surface slope inverted from 3D displacement. The standard deviation of the slip-surface slope is estimated based on the error propagation law:

$$m_\delta^2 = \left(\frac{\partial\delta}{\partial v_N}\right)^2 m_N^2 + \left(\frac{\partial\delta}{\partial v_E}\right)^2 m_E^2 + \left(\frac{\partial\delta}{\partial v_U}\right)^2 m_U^2 \tag{6}$$

where m indicates the standard deviation. Subsequently, we obtain the following equation, based on Eq. (5) and Eq. (6):

$$m_\delta^2 = \left(\frac{v_U v_N}{(v_N^2 + v_E^2 + v_U^2)\sqrt{v_N^2 + v_E^2}}\right)^2 m_N^2 + \left(\frac{v_U v_E}{(v_N^2 + v_E^2 + v_U^2)\sqrt{v_N^2 + v_E^2}}\right)^2 m_E^2 + \left(\frac{\sqrt{v_N^2 + v_E^2}}{v_N^2 + v_E^2 + v_U^2}\right)^2 m_U^2 \tag{7}$$

Eq. (7) shows that the precision of the slip-surface slope is related to the magnitude and precision of the 3D displacement. Therefore, it is difficult to obtain a reliable slip-surface slope for the landslides in a near north–south direction.

2.4. 2D basal-surface and volume estimation

Based on the vector inclination method, the 2D slip-surface can be inferred using the 3D landslide displacement (Carter & Bentley, 1985; Intrieri et al., 2020). This method uses the location of the backscarp or the toe of the rupture surface of the landslide to infer the depth of the entire slip-surface (e.g. (Baum et al., 1998; Intrieri et al., 2020)). The back-scars and toes of the landslides can be identified based on displacement, DEM, and Google Earth images. Unlike the traditional method based on discrete measurements, in this study, continuous 3D displacement fields were used to infer the slip-surface. Based on the slip-surface slope along the central axis of the landslide, the elevation of the slip-surface along the profile can be estimated by the integral, starting from the bottom or the top of the landslide:

$$Z_{s,i} = Z_t - \sum_{top}^{i} P tan\delta \text{ or } Z_{s,i} = Z_b + \sum_{bottom}^{i} P tan\delta \tag{8}$$

where Z represents the elevation; P is the horizontal spacing of the pixels; and the subscripts s, t, and b indicate the slip-surface, top, and bottom of the landslide, respectively, i indicates a position in the horizontal direction. Therefore, two potential slip-surfaces can be inferred from Eq. (8), independently. However, the slip-surface of some landslides may not be completely interconnected at the toe or tail (e.g., (Kang et al., 2019)), and there may be identification errors in the landslide toe and backscarp. Therefore, the slip-surfaces integrated from the bottom and the top may not coincide. In this study, an optimal slip-surface (below the ground-surface, and close to the ground-surface at the two sides) was chosen from the two results.

Many studies have inferred the volume of a landslide using slip-surface geometry (e.g., (Handwerger et al., 2021; Jaboyedoff et al., 2020)). Some of them assume a semi-ellipsoid shape for the slip-surface and infer the volume based on the length, width, and thickness of the landslide (Cruden & Varnes, 1996). Some studies have found that, instead of a semi-ellipsoid, an elliptic paraboloid can reflect the shape of the failure surface more realistically (Jaboyedoff et al., 2020). Therefore, after the landslide depth of the central axis was acquired, an elliptical paraboloid-based model was used to infer the landslide volume.

$$V = \frac{\pi}{8} W_r L_{rh} h_{\max} \tag{9}$$

where V is the landslide volume and W_r, L_{rh}, and h_{max} represent the width, horizontal length, and maximum vertical depth of the landslide, respectively. Because the elliptical paraboloid is symmetrical, we set h_{max} as the maximum vertical depth at the landslide central axis.

3. Results and analyses

3.1. InSAR measurements and identified landslides

To verify the effectiveness of the unwrapping error correction method designed in this study, we manually selected the correctly unwrapped interferograms of two landslides with large displacements in the study area. We then estimated the linear displacement rate of these two landslides based on the original, corrected, and selected interferograms. As shown in Fig. 6, our method can effectively detect and correct unwrapping errors and reduce the impact of unwrapping errors on the results in the study area. However, it should be noted that the phase-closure-based method fails when the displacement of the landslide is too large to be unwrapped, even with the shortest temporal baseline. Therefore, this method often requires prior knowledge. We can judge the applicability of this method by checking the unwrapped phase of the interferograms with the shortest temporal baselines. For example, we checked that the phases of most landslides in the study area could be correctly unwrapped for a time separation of 12 days.

Through the segment processing, the InSAR measurements from the ascending and descending datasets were acquired (Fig. 7). Based on the line-of-sight (LOS) linear displacement rates, SRTM, and Google Earth images of the study area, 50 creeping landslides were identified and numbered. The areas of these delineated landslides were then estimated (Fig. 7). The largest landslide area was 1.402 km^2, and the smallest one was 0.0518 km^2. It should be noted that there is an evident displacement in the area outlined by the dashed rectangle in Fig. 7 where a cluster of landslides exist; however, owing to the dense and continuous displacement in this area, it is difficult to distinguish the boundaries of the individual landslides. Therefore, we did not number the landslides in this area.

Many landslides occur along the Jinsha River Valley, where large elevation variations in the river valley and severe river erosion make it prone to landslides. Besides, the landslides exhibit the spatial distribution characteristics of small-scale clusters (2–4 landslides gathered in each region), which may result from similar geological and topographical conditions. Some of the identified landslides were also detected by Zhao et al. (Zhao et al., 2018) based on ALOS data, including the Dacun-Fujiapingzi landslide (No. 14), Dapingdi landside (No. 16), Jinpingzi landslide (No. 19), Shuanglongtan debris flow (No. 20), and Pufu landslide (No. 24). However, we revealed several landslides that were not identified previously. The improvement in our results can be explained by two main reasons: (1) In this study, both ascending and descending tracks Sentinel-1 data were used for landslide identification, allowing more landslides to be detected than only single track SAR images; and (2) the SAR acquisition periods are different, and landslides often experience different activity in different periods. Therefore, multi-track and long-term SAR datasets are critical to detect more complete landslides through InSAR.

3.2. 3D displacement

The 3D displacement of a landslide provides crucial data support for the inversion of the slip-surface slope. The precision of the 3D displacement directly affects the slip-surface slope estimation (Eq. 7). Thus, using Eq. (3) and (4), we calculated the 3D displacements and their corresponding standard deviations, respectively. The 3D

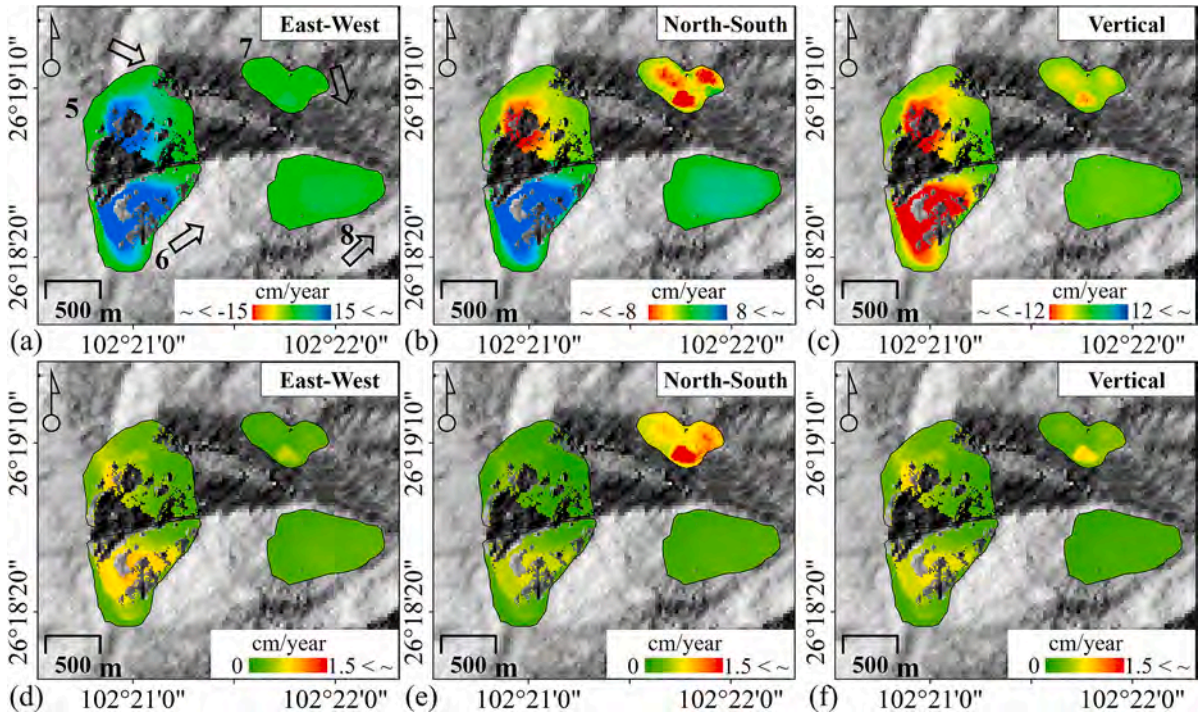

Fig. 8. (a-c) 3D displacement of exemplary landslides. (d-f) Standard deviation of the 3D displacement. (a, d) East-West displacement, with eastward positive. (b, e) North-South displacement, with northward positive. (c, f) Vertical displacement, with the upward positive. The arrow indicates the sliding direction of the landslide. The background is DEM, and the displacements outside the landslide are masked out. The landslide number is shown beside the landslide.

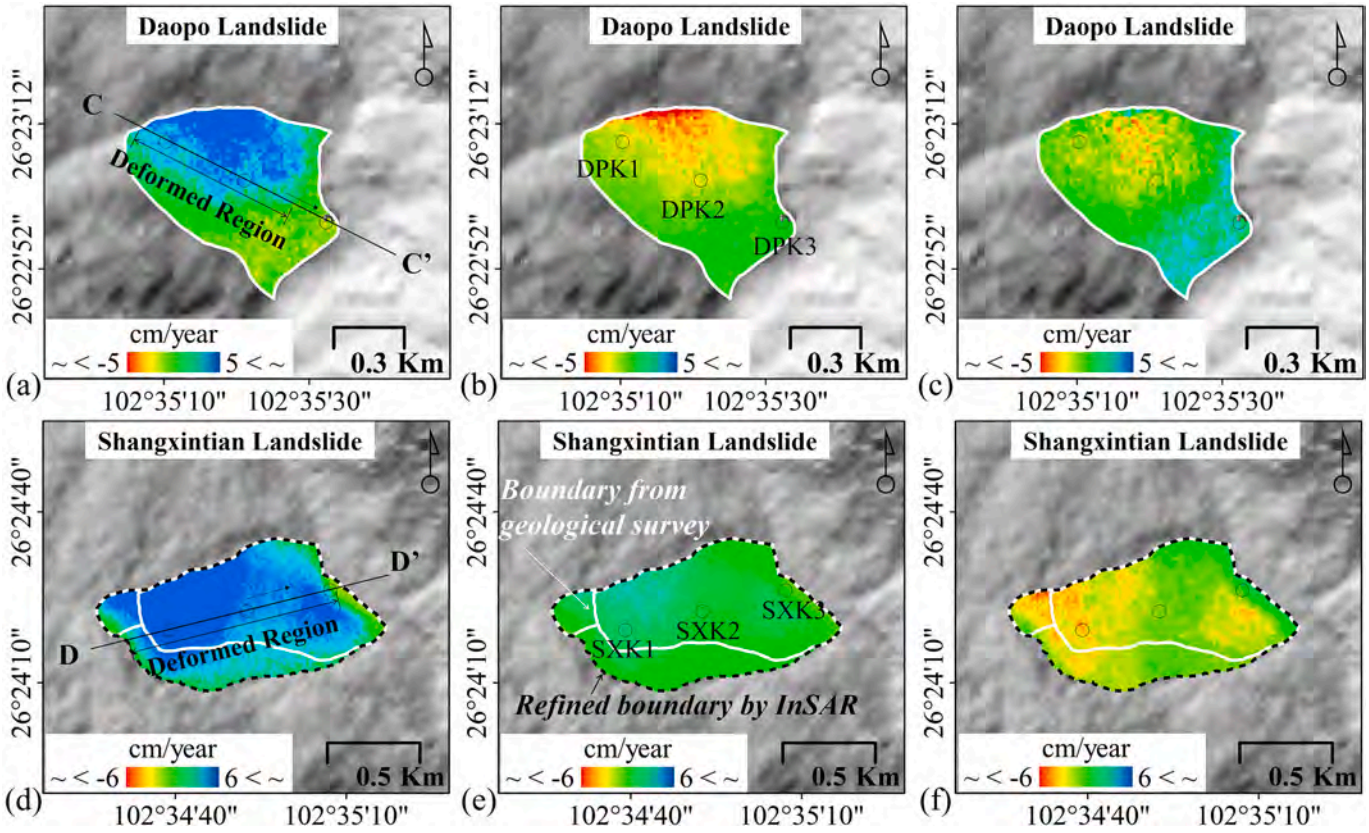

Fig. 9. East-west displacement of (a) Daopo and (d) Shangxintian landslides, with eastward positive; north-south displacement of (b) Daopo and (e) Shangxintian landslides, with northward positive; vertical displacement of (c) Daopo and (f) Shangxintian landslides, with the upward positive. The background is DEM, and the displacements outside the landslide are masked out. The circle indicates the location of the borehole.

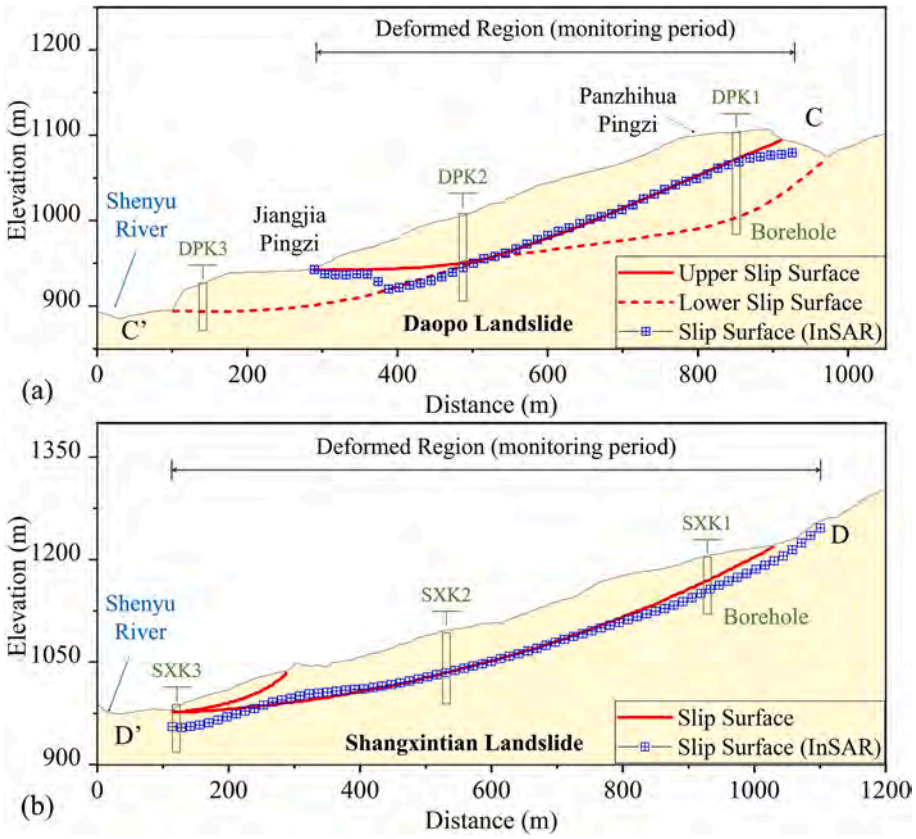

Fig. 10. The sections of (a) Daopo and (b) Shanxintian landslides; the red curve shows the slip-surface inferred from the geological survey, the blue curve represents the sliding surface inferred from the InSAR results, and the green rectangle represents the geological borehole. The locations of the profiles CC' and DD' are shown in Fig. 9. (For interpretation of the references to colour in this figure legend, the reader is referred to the web version of this article.)

displacements of most landslides are continuous in space, and the vertical displacement is typically smaller than the horizontal displacement. In addition, when the slip direction of the landslide was closer to the north–south direction, the uncertainty becomes larger. For example, the slip direction of landslide No. 7 is closer to the north–south direction than those of surrounding landslides (approximately 164°). The standard deviations of the displacements in north–south direction were significantly higher than those of the surrounding landslides (Fig. 8). Moreover, the relative standard deviations of the landslide displacements in other directions were larger than those of the surrounding landslides.

3.3. Evaluation of inferred results

To evaluate the inferred slip-surfaces, we collected and digitized the geological sections of the two landslides in the study area from Hu (Hu, 2014) and Teng (Teng, 2022). These are the Shangxintian (landslide No. 15) and Daopo landslides (landslide No. 17), and their 3D displacements are shown in Fig. 9. We found that some areas outside the Shangxintian landslide extent obtained from geological surveys displayed remarkable deformation; therefore, the landslide boundary was refined based on InSAR measurements.

We compared the slip-surfaces inferred by InSAR with those inferred from geological surveys (borehole and field investigation) (Fig. 10). The borehole data revealed that the Daopo landslide had multiple slip-surfaces. Our results were in good agreement with the upper slip-surface of this landslide. Based on the displacement results, we inferred that this is because the Daopo landslide mainly slid along the upper slip-surface during the monitoring period. For the Shangxintian landslide, the slip-surface inferred in this study is generally consistent with that acquired by the geological survey. However, our method did not reveal the secondary slip-surface at the front of the landslide. In comparison, we suggest that the method proposed in this study can acquire reliable geometric information on the active slip-surface. However, for landslides with multiple slippages, the proposed method cannot detect all slip-surfaces.

Table 1
The Landslide Volume inferred by InSAR and geologic survey.

Number	Landslide Name	InSAR-based ($m^3 \times 10^4$)	Geologic Survey ($m^3 \times 10^4$)
15	Shangxintian	1678	1500 (Teng, 2022), 2000 (Tian, 2009)
16	Dapingdi	7603	6160 (Tian, 2009)
17	Daopo	1627	2460 (Teng, 2022), 2580 (Tian, 2009)
19	Jinpingzi	3473	2700 (Wang et al., 2014)

As shown in Table 1, the landslide volumes estimated in this study were compared with those estimated through geological surveys. Most traditional methods estimate the volume of the creeping landslide based on its geometric information (such as length, width and thickness), thus researchers may obtain different results even for the same landslide. The difference between the two results is not significant, which shows that our method can reveal the landslide volume to a certain extent.

3.4. Slip-surface geometry and volume

Based on Eqs. (5) and (7), we inverted the slip-surface slopes of the landslides and their corresponding standard deviations. We found that the slip-surface slopes of most of the landslides were continuous in space, and the spatial characteristics of the slip-surface slopes varied

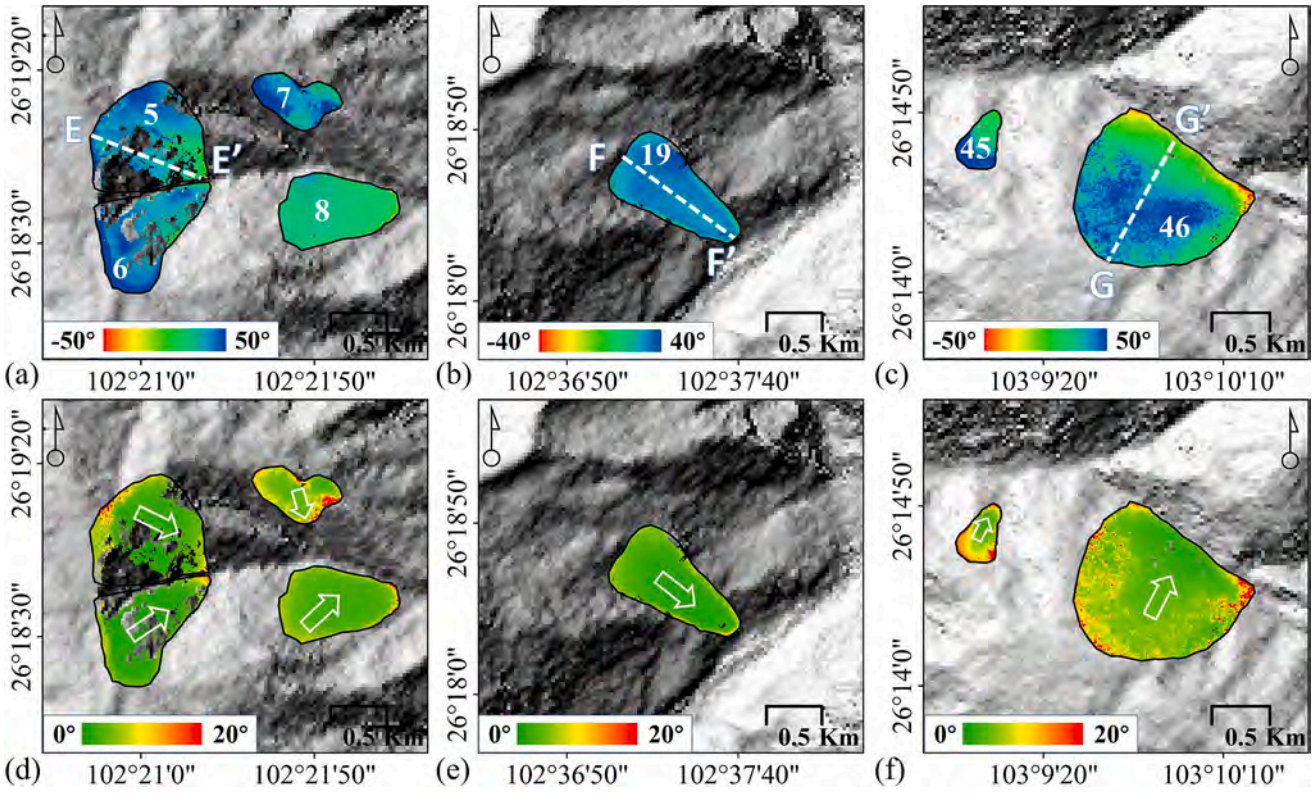

Fig. 11. (a-c) Inverted slip-surface slopes for typical landslides. The landslide number is shown in each landslide. (d-f) Corresponding Standard deviations of these slip-surface slopes, where the arrow indicates the slip direction of the landslide.

among landslides (Fig. 11). And some of the landslides' slip-surfaces were approximately parallel to the ground surface. There were differences of tens of degrees between the slip and ground surfaces in some areas (Fig. 11). Many of the slope differences were much larger than the standard deviations of the slip-surface slopes (as shown in Fig. 12), which certify that slip-surface cannot be parallel to ground-surface. Hence, the traditional projection of InSAR measurements in the ground surface gradient direction as done in most of the previous studies is inaccurate.

In some landslides, the slip-surface slope became negative at the toe of the landslide (Fig. 12). According to the conceptual model (Fig. 5), a negative slope indicates that the slip-surface is curved upward. While, in some other landslides, the slip-surface slope changes little in space, indicating that the slip-surface was approximately an inclined plane.

Owing to the great uncertainty in the slip-surface slopes of some landslides facing north-south, 30 landslides were selected for further processing. We inferred the depths of the slip-surfaces of these landslides using Eq. (8) (some of the results are shown in Fig. 12). The maximum and average vertical depths along the central axis of these landslides ranged from 30 to 249 m and from 16 to 160 m, respectively. The volumes of these landslides were inferred using Eq. (9), which ranged from 483,412 to 135,789,944 m^3.

The 2D slip-surface also shows potential in landslide classification. An upward curved (or spoon-shaped) slip-surface is a typical feature of a rotational landslide, whereas a typical feature of a translational landslide is that the slip-surface is approximately parallel to the ground surface. As shown in Fig. 11 and 12, for landslide No.19, the profile of the slip-surface was similar to an inclined straight line, and the slope of the slip-surface was similar to that of the ground surface. Therefore, we deduced that landslide No. 19 was a typical translational landslide. For landslide No. 46, the slip-surface slope was larger than the surface slope in the rear section and smaller than the surface slope in the front section. The entire slip-surface profile of landslide No. 46 is an upward curved arc (spoon-shaped), indicating that it is a typical rotational landslide.

4. Discussion

4.1. Uncertainty analysis

4.1.1. Displacement precision

The precision of the displacement has a direct impact on the quality of the inverted slip-surface geometry. As shown in Fig. 13, the mean standard deviations of the displacement rates from all the datasets were <5 mm/year. As the incidence angles of the InSAR measurements from the ascending and descending tracks are similar in the study area, the deformation difference between the ascending and descending datasets in the flat region (the region with a slope angle smaller than 5° in this study) was used to form the histograms. The standard deviation of the deformation difference was 8.7 mm/year (Fig. 13). The above analysis on precision shows that our InSAR results are reliable.

However, even if high-precision measurement can be acquired by InSAR, it is still difficult to invert the accurate three-dimensional displacements of the landslide when the slip direction of the landslide is closer to the north–south direction. This is because the design matrix in Eq. (3) is ill-conditioned when the slope aspect is closer to the north–south direction, which amplifies the error in the InSAR observation. Compared with other directions, more accurate 3D displacement can be inverted by Eq. (3) when the slope aspect is close to the east-west direction. In addition, the slope aspect was used to restrict the slip direction of the landslide in the 3D displacement inversion. However, it remains possible that the slope aspect is not consistent with the aspect of the failure surface in some cases (Ren et al., 2022). Thus, the error of the inversion model affects the accuracy of the results as well. Therefore, we suggest that more InSAR measurements with independent LOS geometry (e.g., the left-looking NASA-ISRO Synthetic Aperture Radar (NISAR) are needed for the accurate inversion of 3D displacements.

4.1.2. Slip-surface geometry uncertainty

In addition to the displacement errors, the change in landslide

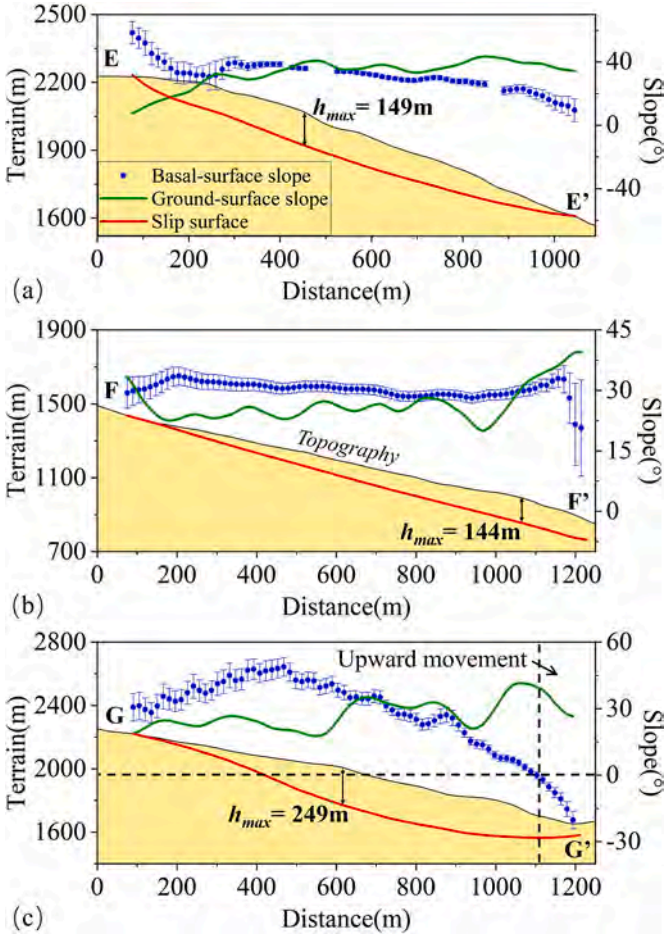

Fig. 12. Cross-sections of terrain and slip-surface elevations, and ground-surface and slip-surface slopes. The locations of these profiles are shown in Fig. 11. The error bars represent 2 standard deviations of the slip-surface slope. The legend in subfigure (a) applies to all the subfigures.

thickness is another factor affecting the accuracy of the inferred slip-surface geometries. This is because Eq. (5) does not consider landslide thickening and thinning. We need to evaluate the extent to which slope-normal deformation (thickening and thinning) affects the inverted slip-surface slope (Baum et al., 1998; Jaboyedoff et al., 2020). Some researchers have reported that landslides may exhibit periodic thickening and thinning. For example, Hu et al. (Hu et al., 2016) found that a slight periodic vertical deformation exists in the Crescent Lake landslide through GPS and InSAR measurements. They suggested that it could be an elastic loading deformation caused by the accumulated mass of infiltrated rainfall (Hu et al., 2016). Kang et al. (Kang et al., 2021) also found that landslides in the Eldorado National Forest may exhibit slight upward or downward deformations owing to unloading and loading effects caused by precipitation. In addition, a periodic dilation (up to a few centimeters of vertical deformation) is expected in clay-rich shear zones in seasonal landslides (Booth et al., 2020; Iverson, 2005), and the recovery of this dilation may be attributed to the dry season soil consolidation and desiccation (Iverson, 2005). To address these fluctuations, the linear deformation rate that suppresses the effect of periodic deformation was estimated and used in this study.

Moreover, with these movements, a landslide thins irregularly in the stretching areas and thickens in the shortening areas (Baum et al., 1998). Therefore, to explore the deformation caused by the stretching and shortening of the landslides, based on the 3D displacements derived by Eq. (3), we calculated the 2D dilation and shear rates for the landslides using Eqs. (10) and (11), respectively.

$$e_S = \frac{1}{2}\left(\frac{\partial v_N}{\partial E} + \frac{\partial v_E}{\partial N}\right) \tag{10}$$

$$e_D = e_N + e_E = \frac{\partial v_N}{\partial N} + \frac{\partial v_E}{\partial E} \tag{11}$$

where e_S indicates the 2D shear rate and $e_D$indicates the 2D dilation rate. In the study area, we selected several landslides with relatively large displacements to reveal the strain characteristics (Fig. 14).

The shear strain mainly occurs along the two side boundaries, which is similar to that of strike-slip faulting. The front section of the landslide tends to be compressed and the rear section tends to be dilated. Based on the 2D strain, the thinning/thickening caused by the stretching/shortening of the landslides could be inferred. We assume that a landslide is sliding along a slip-surface, and the schematic diagram of the thickness changes of a vertical prism above the slip-surface is shown in Fig. 15.

The volume of the landslide can be assumed to be constant during the creeping, which has been verified in many cases (e.g. (Booth et al., 2020; Handwerger et al., 2021)). The ΔE and ΔN represent the spacing of the prism in the east-west and north-south directions. Then, the e.q. (12) can be derived,

$$\Delta E \cdot \Delta N \cdot h = (\Delta N + e_N \Delta N)(\Delta E + e_E \Delta E) \cdot (h + \Delta h) \tag{12}$$

where h is the thickness of the prism, $\triangle h$ indicates the thickness changes in the vertical direction, and $e_E \Delta E$ and $e_N \Delta N$ represent the stretching/shortening of the prism in the east-west and north-south directions. In this study, $\Delta E = \Delta N \approx 15(m)$, and $e_N e_E \approx 0$, then the e.q. (13) can be derived,

$$\Delta h = \frac{h}{1 + e_D} - h \tag{13}$$

We found that, in most of these landslides, the stretching/shortening was much smaller than the downslope sliding (displacement) of the landslide. For example, the maximum longitudinal stretching/shortening rate of the Dapingdi landslide was approximately 3 cm/year (Fig. 14), and the stretching/shortening in most areas of this landslide was <1 cm/year. However, the maximum sliding rate of this landslide reached 40 cm/year. As the thickness of a landslide is tens of meters, we infer that length changes may cause annual millimeter- or centimeter-level vertical thickening and thinning in most sections of the landslide.

To provide a quantitative evaluation of the results, we assume that the slip-surface slope of a landslide was 30°. The sliding rate along the slip-surface was 20 cm/year and the maximal annual thinning reached 2 cm at the rear of the landslide. We then inferred that the slope of the slip-surface was 35.7° using Eq. 5. For a horizontal distance of 15 m (about one-pixel spacing), this slope error (5.7°) will cause an error of 2.1 m in the slip-surface depth estimation. Considering that the obvious thickening and thinning mainly occurred in localized regions, we concluded that the thickness changes have limited influence on the estimated slip-surface geometry in this study.

4.2. Landslide statistics

We calculated the average slope of the ground surface, the average slip rate, and the area of the 50 creeping landslides. The average downslope sliding rate of these landslides ranged from 2.4 to 26.6 cm/year, and the average downslope sliding rate of most of them was <10 cm/year. InSAR is limited by noise and it is therefore difficult to detect landslides with very small deformation. In addition, we masked out the measurements in the shadow and layover regions where accurate InSAR observations cannot be obtained. Therefore, there may be landslides in the shadow and layover regions or with lower average slip rates that have not yet been found in this study. As shown in Fig. 16, the number of landslides peaked at an average slip rate of 5 cm/year, and the number of landslides with an average slip rate of 5–25 cm/year gradually

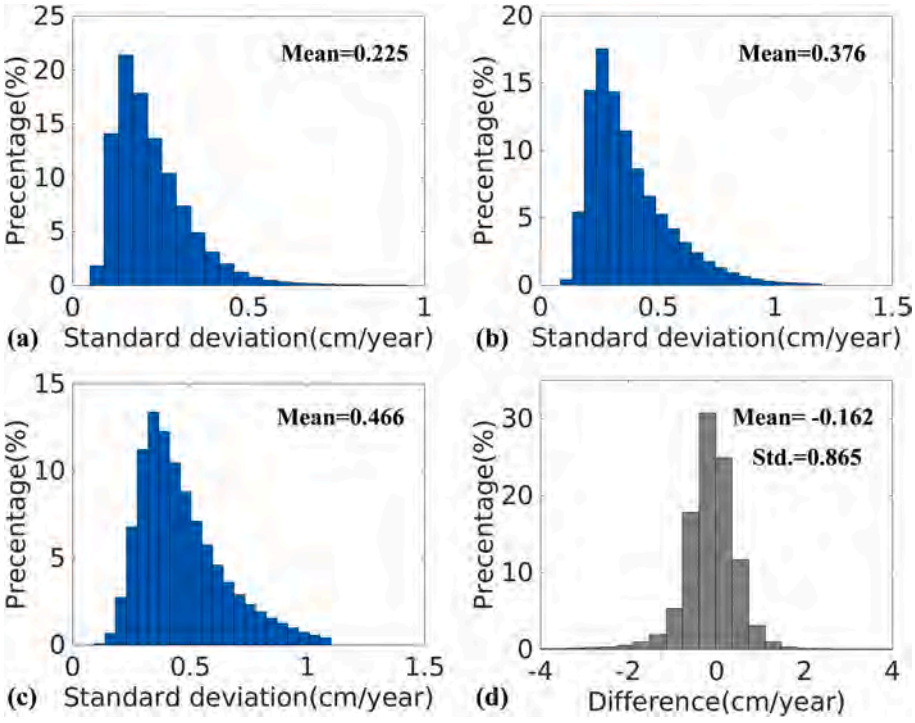

Fig. 13. (a-c) The histogram of the standard deviation of the InSAR measurements. (a) Descending datasets; (b) Ascending datasets on the west side; (c) Ascending datasets on the east side; (d) Displacement rate difference between ascending and descending datasets in the flat regions.

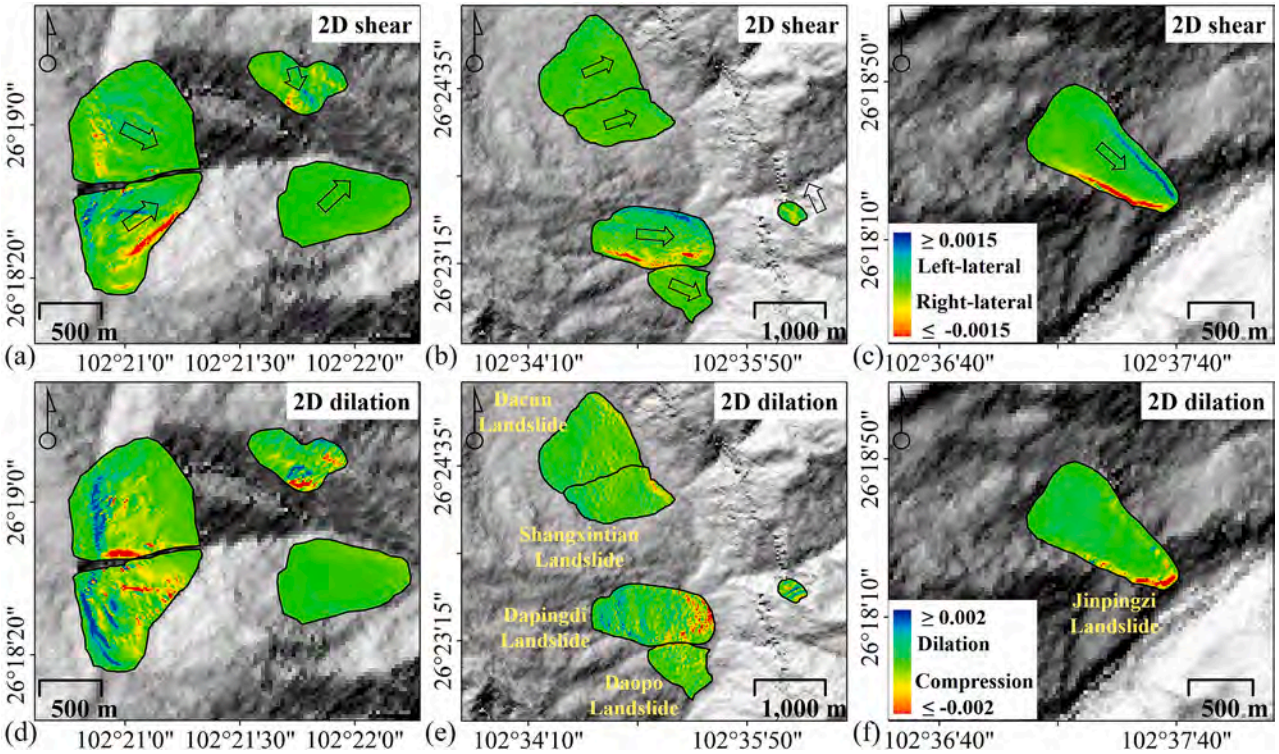

Fig. 14. Maps of (a-c) 2D shear strain rate and (d-f) 2D dilation strain rate computed from the 3D displacement field of some exemplary landslides with relatively large displacements in the study area. The arrow indicates the sliding direction of the landslide. The background is DEM, and the strain rates outside the landslide are masked.

decreased. The average ground-surface slopes were mainly distributed between 30° and 35°. The minimum and maximum average ground-surface slopes were 14° and 40°, respectively. However, steep ground-surface slopes can cause shadows or layovers owing to the SAR imaging geometry; therefore, there may be extra sections of landslides with larger ground-surface slopes. The areas of many landslides were between 5×10^4 and 3.6×10^5 m^2. We did not find any apparent relationship between the surface slope and slip rate or any clear relationship between the ground-surface slope and the slip rate.

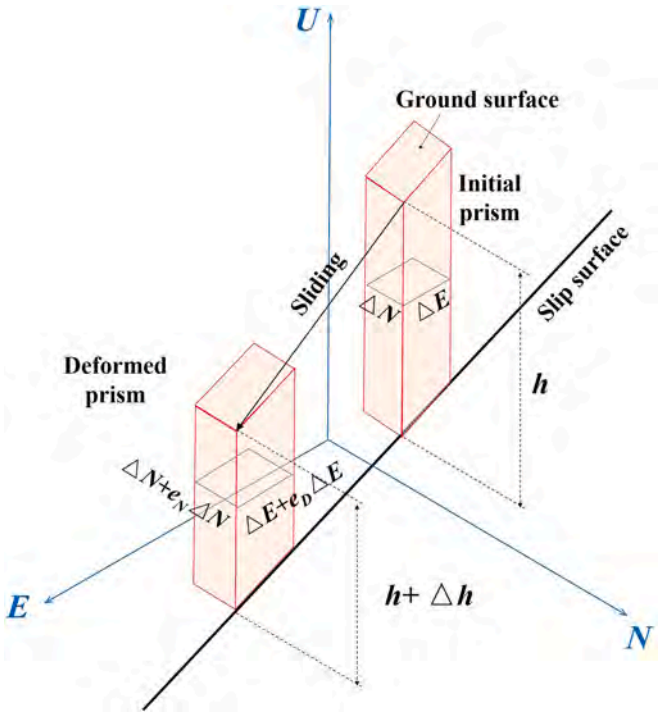

Fig. 15. The schematic diagram of the landslide thickness changes caused by the stretching/shortening of the landslide (modified after (Baum et al., 1998)).

4.3. Scaling of landslide area and volume

Many scholars have attempted to use a power-law function to describe the relationship between landslide volume and area. The parameters of the power-law function are crucial for quantifying regional landslide erosion and understanding landslide mechanisms:

$$V = k \times A^{\alpha} \tag{14}$$

where V represents landslide volume, A represents landslide area, k is a constant, and α is an exponent. Based on the volume and the area of the 30 selected landslides, we can obtain the best-fitting function $V = 0.002 \times A^{1.744}$. We collected some empirical relationships from the literature and compared them with our findings (as shown in Fig. 17). Guzzetti et al. (Guzzetti et al., 2009) used a worldwide catalog of landslides to acquire the relationship $V = 0.074 \times A^{1.450}$ (straight red line in Fig. 17). Most of the landslides in this study tend to have larger volumes per area compared with this model. This phenomenon can be explained by the fact that most of the landslides identified in this study were deep-seated landslides, which was verified by their inferred slip-surface depths. In addition, the area–volume relationships of several identified landslides showed good agreement with those of the bedrock landslides in Larsen et al. (Larsen et al., 2010). This phenomenon may indicate that some landslides detected in this study are deep-seated bedrock landslides.

5. Conclusions

To acquire slip-surface geometries and volumes of landslides in an area of the Jinsha River Basin, a set of processing strategies using InSAR have been developed. A phase-closure-based method was designed to correct the InSAR phase-unwrapping errors caused by the large gradient displacement in the study area. InSAR segment processing was used to determine the local surface displacement over the mountainous area and steep gorges in the Jinsha River basin. Based on the InSAR measurements, Google Earth images and topography, 50 creeping landslides were detected. Subsequently, the 3D displacements of the landslides and the corresponding standard deviations were estimated. Based on the assumption that the landslide displacement is parallel to the slip-surface, we designed a method to invert the slip-surface slope of the landslides through 3D displacement and discussed the accuracy and precision of the inversion. The results show that there may be a significant difference between the ground-surface slope and slip-surface slope in some landslides and that the characteristics of the slip-surface slope can reflect the slip-surface geometry to a certain extent. Using the slip-surface slope data and an ellipsoid paraboloid model, the slip-surface depths and volumes of the 30 selected landslides were estimated. A comparison with the in-situ data suggests that the slip-surface and volume acquired in this study are reliable. However, our method cannot reveal all the slip-surfaces of a landslide with multiple slippages. The average depth of the central axis of these landslides was 16–160 m, and the landslide volumes ranged from 483,412 to 135,789,944 m^3.

We found that the average slip rates of the identified landslides were mainly distributed at approximately 5 cm/year, the average ground-surface slopes were mainly distributed between 30° and 35°, and the

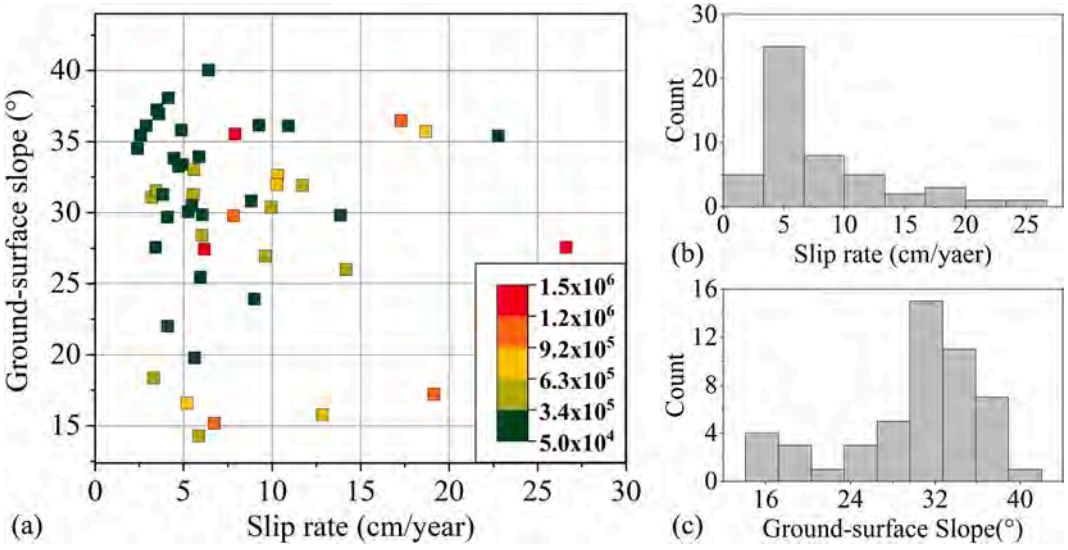

Fig. 16. (a) Comparison of the ground-surface slope, average slip rate, and area of landslides. The colour indicates the landslide area and the unit of the colour bar is m^2. (b) The histogram of the average slip rate of the detected landslides. (c) The histogram of the ground-surface slope of the detected landslides.

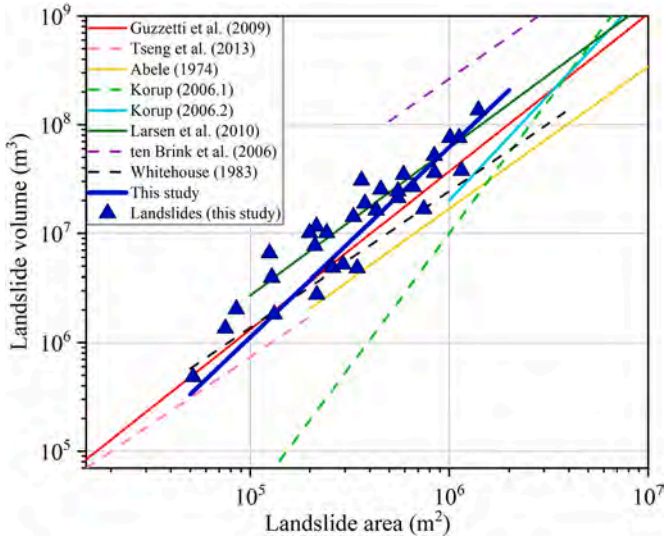

Fig. 17. Relationships between the area and volume of the 30 landslides, and surface area–volume power laws from different literature. Guzzetti et al. (Guzzetti et al., 2009)—World synthesis; Tseng et al. (Tseng et al., 2013)—Typhoon Marakot landslide; Abele (Abele, 1974)—Deep-seated landslide in the European Alps; (Korup, 2006)—Landslides in SW New Zealand (> 0.02 km^2); (Korup, 2006)—Landslides in SW New Zealand (> 1 km2); Larsen et al. (Larsen et al., 2010)—Bedrock landslides; ten Brink et al. (ten Brink et al., 2006)—Submarine landslides; Whitehouse (Whitehouse, 1983)—Deep-seated landslides in the Central Southern Alps.

areas of the landslides were mostly $<3.6 \times 10^5$ m^2. In addition, a power-law function was used to describe the relationships between landslide area and volume in the region. Compared with the relationships obtained in other studies, we suggest that deep-seated landslide is the main landslide type in the study area. Further, the area extents, volumes, slip-surface geometries of the landslides obtained in this research are critical to enhance the understanding of the landslides in the study area and provide new insights into landslide mechanisms.

CRediT authorship contribution statement

Ya Kang: Methodology, Software, Formal analysis, Data curation, Funding acquisition, Writing – original draft, Writing – review & editing. **Zhong Lu:** Conceptualization, Writing – review & editing. **Chaoying Zhao:** Formal analysis, Resources, Funding acquisition, Writing – review & editing. **Wei Qu:** Resources, Writing – review & editing.

Declaration of Competing Interest

The authors declare that they have no known competing financial interests or personal relationships that could have appeared to influence the work reported in this paper.

Data availability

Data will be made available on request.

Acknowledgments

The authors would like to thank the European Space Agency for providing the Sentinel-1A/B and the Sentinel-2 data freely. One-arc-second SRTM DEM was freely downloaded from the website http://e4ftl01.cr.usgs.gov/MODV6_Dal_D/SRTM/. This research was funded by the National Natural Science Foundation of China (Grant No. 41929001, 41874005, 42174006), National Key R&D Program of China (No.2022YFC3004302), Natural Science Research Start-up Foundation of Recruiting Talents of Nanjing University of Posts and Telecommunications (Grant No. NY221140), Science Fund for Distinguished Young Scholars of Shaanxi Province (Grant No. 2022JC-18), and the Shuler-Foscue Endowment at Southern Methodist University.

References

Abele, G., 1974. Bergsturze in Den Alpen ihre verbreitung, morphologie und folgeerscheinungen. Wiss. Alpenvereinshefte 25 (230p).
Baum, R.L., Messerich, J., Fleming, R.W., 1998. Surface deformation as a guide to kinematics and three-dimensional shape of slow-moving, clay-rich landslides, Honolulu,Hawaii. Environ. Eng. Geosci. 4 (3), 283–306.
Bekaert, D.P.S., Hooper, A., Wright, T.J., 2015. A spatially variable power law tropospheric correction technique for InSAR data. J. Geophys. Res. Solid Earth 120 (2), 1345–1356.
Bishop, K.M., 1999. Determination of translational landslide slip-surface depth using balanced cross sections. Environ.Eng.Geosc. 2, 147–156.
Booth, A.M., McCarley, J.C., Nelson, J., 2020. Multi-year, three-dimensional landslide surface deformation from repeat lidar and response to precipitation: Mill Gulch earthflow,California. Landslides 1–14.
Carter, M., Bentley, S.P., 1985. The geometry of slip-surfaces beneath landslides: predictions from surface measurements. Can. Geotech. J. 22 (2), 234–238.
Crippa, C., Valbuzzi, E., Frattini, P., Crosta, G.B., Spreafico, M.C., Agliardi, F., 2021. Semi-automated regional classification of the style of activity of slow rock-slope deformations using PS InSAR and SqueeSAR velocity data. Landslides 18 (7), 2445–2463.
Cruden, D.M., Varnes, D.J., 1996. Landslide types and processes. In: Turner, A.K., Schuster, R.L. (Eds.), Landslides: Investigation and Mitigation (Special Report). 247. National Research Council, Transportation and Research Board Special Report, Washington, DC, USA, pp. 36–75.
Guzzetti, F., Ardizzone, F., Cardinali, M., Rossi, M., Valigi, D., 2009. Landslide volumes and landslide mobilization rates in Umbria, Central Italy. Earth Planet. Sci. Lett. 279 (3–4), 222–229.
Handwerger, A.L., Booth, A.M., Huang, M.H., Fielding, E.J., 2021. Inferring the subsurface geometry and strength of slow-moving landslides using 3-D velocity measurements from the NASA/JPL UAVSAR. J Geophys.Res.Earth Surf. 126 (3) e2020JF005898.
Hu, Q., 2014. Study on Landslide Hazards Risk of Wudongde Bank. [D] Changjiang River Scientific Research Institute, Wuhan, China.
Hu, X., Wang, T., Pierson, T.C., Lu, Z., Kim, J., Cecere, T.H., 2016. Detecting seasonal landslide movement within the Cascade landslide complex (Washington) using time-series SAR imagery. Remote Sens. Environ. 187, 49–61.
Hu, X., Lu, Z., Pierson, T.C., Kramer, R., George, D.L., 2018. Combining InSAR and GPS to determine transient movement and thickness of a seasonally active low-gradient translational landslide. Geophys. Res. Lett. 45 (3), 1453–1462.
Huang, B., Yin, Y., Liu, G., Wang, S., Chen, X., Huo, Z., 2012. Analysis of waves generated by Gongjiafang landslide in Wu Gorge, three Gorges reservoir, on November 23, 2008. Landslides 9 (3), 395–405.
Intrieri, E., Frodella, W., Raspini, F., Bardi, F., Tofani, V., 2020. Using satellite interferometry to infer landslide sliding surface depth and geometry. Remote Sens. 12 (9), 1462.
Iverson, R.M., 2005. Regulation of landslide motion by dilatancy and pore pressure feedback. J.Geophys.Res.Earth Surf. 110 (F2).
Jaboyedoff, M., Carrea, D., Derron, M.H., Oppikofer, T., Penna, I.M., Rudaz, B., 2020. A review of methods used to estimate initial landslide failure surface depths and volumes. Eng. Geol. 267, 105478.
Kang, Y., Lu, Z., Zhao, C., Zhang, Q., Kim, J.W., Niu, Y., 2019. Diagnosis of Xinmo (China). Remote Sensing 11 (16), 1846.
Kang, Y., Lu, Z., Zhao, C., Xu, Y., Kim, J.W., Gallegos, A.J., 2021. InSAR monitoring of creeping landslides in mountainous regions: a case study in Eldorado National Forest,California. Remote Sens. Environ. 258, 112400.
Korup, O., 2006. Effects of deep-seated bedrock landslides on hillslope morphology, southern Alps, New Zealand. J. Geophys. Res. 111, F01018.
Kruskal, J.B., 1956. On the shortest spanning subtree of a graph and the traveling salesman problem. Proc. Am. Math. Soc. 7 (1), 48–50.
Larsen, I.J., Montgomery, D.R., Korup, O., 2010. Landslide erosion controlled by hillslope material. Nat. Geosci. 3 (4), 247–251.
Lauknes, T.R., Zebker, H.A., Larsen, Y., 2010. InSAR deformation time-series using an L1-norm small-baseline approach. IEEE Trans. Geosci. Remote Sens. 49 (1), 536–546.
Liu, X., Zhao, C., Zhang, Q., Yin, Y., Lu, Z., Samsonov, S., Tomás, R., 2021. Three-dimensional and long-term landslide displacement estimation by fusing C-and L-band SAR observations: a case study in Gongjue County, Tibet,China. Remote Sens. Environ. 267, 112745.
Lu, Z., Kim, J.W., 2021. A framework for studying hydrology-driven landslide hazards in northwestern US using satellite InSAR. Precipitation and Soil Moisture Observations: Early Results and Future Directions, GeoHazards 2 (2), 17–40.
Ren, K., Yao, X., Li, R., et al., 2022. 3D displacement and deformation mechanism of deep-seated gravitational slope deformation revealed by InSAR: a case study in Wudongde Reservoir, Jinsha River. Landslides 19 (9), 2159–2175.
Saroli, M., Albano, M., Atzori, S., Moro, M., Tolomei, C., Bignami, C., Stramondo, S., 2021. Analysis of a large seismically induced mass movement after the December 2018 Etna volcano (southern Italy) seismic swarm. Remote Sens.Environ. 263, 112524.

Schlögel, R., Doubre, C., Malet, J.P., Masson, F., 2015. Landslide deformation monitoring with ALOS/PALSAR imagery: a D-InSAR geomorphological interpretation method. Geomorphology 231, 314–330.

ten Brink, U.S., Geist, E.L., Andrews, B.D., 2006. Size distribution of submarine landslides and its implication to tsunami hazard in Puerto Rico. Geophys. Res. Lett. 33, 23–26. https://doi.org/10.1029/2006GL026125.

Teng, M., 2022. On the Formation Mechanism and Stability Assessment of Landslide Group on the Right Bank of Trevally River in the Reservoir Area of Wudongde Hydropower Station. [D] China Three Gorges University, Wuhan, China.

Tian, W., 2009. Analysis on Influence of Debris Flow at Near-dam Reservoir Bank of Wudongde Hydropower Station. [D] Jilin University, Jilin, China.

Tseng, C.M., Lin, C.W., Stark, C.P., Liu, J.K., Fei, L.Y., Hsieh, Y.C., 2013. Application of a multi-temporal, LiDAR-derived, digital terrain model in a landslide-volume estimation. Earth Surf. Process. Landf. 38 (13), 1587–1601.

Wang, X.M., 2013. Study on Rock Fractures and Rock Blocks in Wudongde Dam Area. China University of Geosciences, Beijing, China. Ph.D. Thesis.

Wang, Z.H., Guo, D.H., Zheng, X.W., Wang, J.C., Guo, Z.C., Dong, L.N., 2011. Remote sensing interpretation on June 28, 2010 Guanling landslide, Guizhou Province, China. Geosci. Front. 18, 310–316 (In Chinese).

Wang, H., Wright, T.J., Yu, Y., Lin, H., Jiang, L., Li, C., Qiu, G., 2012. InSAR reveals coastal subsidence in the Pearl River Delta, China. Geophys.J.Int. 191 (3), 1119–1128.

Wang, T.L., Liu, C.P., Hao, W.Z., 2014. Geological research on Jinpingzi giant landslide of Wudongde Hydropower Station. Yangt. Riv. 45, 54–58 (In Chinese).

Whitehouse, I.E., 1983. Distribution of large rock avalanche deposits in the central southern Alps, New Zealand. N. Z. J. Geol. Geophys. 26 (3), 271–279.

Xu, L.M., 2013. Risk Assessment and Study on Prevention of Debris Flows near the Dam of Wudongde Hydropower Station Based on Catastrophe Theory. Jilin University, Jilin, China.

Xu, Y., Lu, Z., Leshchinsky, B., 2022. Kinematics of irrigation-induced landslides in a Washington desert: impacts of basal geometry. J.Geophys.Res.Earth Surf. e2021JF006355.

Zhao, C., Lu, Z., Zhang, Q., de La Fuente, J., 2012. Large-area landslide detection and monitoring with ALOS/PALSAR imagery data over northern California and southern Oregon, USA. Remote Sens. Environ. 124, 348–359.

Zhao, C., Kang, Y., Zhang, Q., Lu, Z., Li, B., 2018. Landslide identification and monitoring along the Jinsha River catchment (Wudongde reservoir area), China, using the InSAR method. Remote Sens. 10 (7), 993.